Paper Number 127

Prediction of the Rotor Aeromechanics in Descending Flight using Mixed Variational Geometrically Exact Beam Model and CFD Coupled Analysis

Hanyeol Ryu
Graduate Student
School of Mechanical and Aerospace Engineering,
Seoul National University

Seoul, KOREA
klyu21@snu.ac.kr

Dong Ok Yu
Graduate Student
Aerospace Engineering,
Korea Advanced Institute of Science and Technology

Daejeon, KOREA
dyu0404@kaist.ac.kr

SangJoon Shin
Professor
School of Mechanical and Aerospace Engineering,
Seoul National University

Seoul, KOREA
ssjoon@snu.ac.kr

Oh Joon Kwon
Professor
Aerospace Engineering,
Korea Advanced Institute of Science and Technology

Daejeon, KOREA
ojkwon@kaist.ac.kr

Abstract

This paper presents prediction of the rotor aeromechanics for HART II experiment in a descending flight. The HART II was conducted to improve understanding of the Blade-Vortex Interaction (BVI) phenomena. For precise predictions of the aeromechanics of the HART II, CSD/CFD coupled analyses were conducted based on the delta load approach. In the CSD model, the mixed variational geometrically exact beam model was used to obtain the blade nonlinear behavior, and a CFD flow solver based on unstructured meshes was used for predicting the blade aerodynamic loads. The present beam model has advantages that displacements, internal forces/moments, and linear/angular momenta can be obtained directly. For the delta load approach, a finite-state dynamic inflow model was used to analyze trim condition for initial step in the present CSD model. The present results are compared with the measurement on the HART II rotor blades. The structural results show that the predicted flap deflection is quite similar with that of the measurement, but the torsional and lag deflections are under-predicted compared to those of the measurement.

1. Introduction

Higher-harmonic Aeroacoustic Rotor Test (HART) II [1-2] was conducted in 2001 in order to improve understanding of the Blade-Vortex Interaction (BVI) that the tailed tip vortices generated by preceding rotor blades may influence the following blades. The BVI produces unsteady pressure variations with high frequencies on the blades, causing rotor vibration and noise problems. And these phenomena can be presented mainly in low speed translation and maneuver flights. So, the HART II was conducted in low speed descending flights, and the measurement that includes the BVI airloads, blade deflections, and blade structural loads. And the measurement was obtained with and without higher-harmonic pitch control inputs (HHC). In the previous research works, many of the researchers have sought to validate the measurement [3-11] using comprehensive analysis codes such as University of Maryland Advanced Rotorcraft Code (UMARC) [12], Comprehensive Analytical Model of Rotorcraft Aerodynamics and Dynamics (CAMRAD II) [13] or DYMORE [14] with CFD analysis. The structural model in UMARC adopted a geometrically nonlinear but approximated beam formulation which retained terms up to second order by introducing the non-dimensional quantity ε, such that $\varepsilon << 1$. In contrast, CAMRAD II and DYMORE provided a refined beam formulation, which can capture the geometrical nonlinearity using a geometrically exact beam theory with a displacement-based formulation. But, to calculate internal forces and moments, an additional post processing such as force summation method was established. But, in the previous works, it is difficult to find numerical results by using geometrically exact beam model based on mixed variational formulations.

In the present structural model, geometrically exact beam analyses with a mixed variational formulation was adopted [15]. Thus, internal forces and moments, linear and angular momenta, and displacements are

obtained directly and solved simultaneously. The blade aerodynamic loads were obtained from a CFD flow solver based on unstructured meshes. A combination of overset mesh and deforming mesh techniques was used to handle the blade motion including blade deflections.

In this paper, first, the CSD model coupled with an aerodynamic model employing a blade-element method and a finite-state dynamic inflow model [16] was validated against the HART II measurement. Then, fully CSD/CFD coupled analyses were conducted. In the numerical results, the predicted flap deflection shows a good correlation with that of the measurement but, the torsional and lag deflection results are under-predicted. The present CSD/CFD coupled analyses are still ongoing, so, the final results will be shown in the future.

2. Formulation

2.1 CSD analysis

The present CSD model is a geometrically exact beam model based on Hodges's formulation [15] to capture blade nonlinear behavior. It assumes small strain and large deformation with finite rotation. By adopting this formulation, the rotor blades that undergoes large deformation with initially curved and twisted can be analyzed without any geometric simplifying approximation. The variational formulation is derived from Hamilton's principle as follows:

$$\int_{t_1}^{t_2}\int_0^l [\delta(K-U)+\overline{\delta W}]dx_1 dt = \overline{\delta A} \tag{1}$$

Internal forces F_B, M_B and momenta P_B, H_B are obtained from strain and kinetic energies.

$$\int_0^l \delta U dx_1 = \int_0^l \left[\delta\gamma^T {F_B}^T + \delta\kappa^T {M_B}^T\right] dx_1 \tag{2}$$

$$\int_0^l \delta K dx_1 = \int_0^l \left[\delta V_B^T {P_B}^T + \delta\Omega_B^T {H_B}^T\right] dx_1 \tag{3}$$

When the cross section properties of the rotor blades are estimated by using a certain cross sectional analysis, the internal forces and momenta can be obtained as follows:

$$\begin{Bmatrix} F_B \\ M_B \end{Bmatrix} = [S]\begin{Bmatrix} \gamma \\ \kappa \end{Bmatrix}, \quad \begin{Bmatrix} P_B \\ H_B \end{Bmatrix} = [M]\begin{Bmatrix} V \\ \Omega \end{Bmatrix} \tag{4}$$

By substituting the above equations into the eq. (1), eq. (1) can be expressed as follows:

$$\begin{aligned} &\int_{t_1}^{t_2}\int_0^l \left[\delta V_B^{*T} P_B + \delta\Omega_B^{*T} H_B - \left(\delta\gamma^{*T} F_B + \delta\kappa^{*T} M_B\right)\right] dx_1 dt \\ &+\int_{t_1}^{t_2}\int_0^l \overline{\delta W} dx_1 dt = \overline{\delta A} \end{aligned} \tag{4}$$

where * means that V_B^*, Ω_B^*, γ^*, and κ^* satisfy the geometrically exact relationship. In the current "a" frame, such a geometrically exact relationship is defined as follows:

$$\begin{aligned} &\gamma^* = C^{Ba}\left(C^{ab}e_1 + u_a'\right) - e_1 \quad , \quad \kappa^* = C^{ba}\left(\frac{\Delta - \frac{\tilde{\theta}}{2}}{1+\frac{\theta^T\theta}{4}}\right)\theta' \\ &V_B^* = C^{Ba}\left(v_a + \dot{u}_a + \tilde{\omega}_a u_a\right) \quad , \quad \Omega_B^* = C^{ba}\left(\frac{\Delta - \frac{\tilde{\theta}}{2}}{1+\frac{\theta^T\theta}{4}}\right)\dot{\theta} + C^{Ba}\omega_a \end{aligned} \tag{5}$$

The mixed variational formulation will be obtained by substituting eq. (5) into eq. (4), as follows:

$$\begin{aligned} &\int_{t_1}^{t_2}\int_0^l [\delta V_B^{*T} P_B + \delta\Omega_B^{*T} H_B - \delta\gamma_B^{*T} F_B - \delta\kappa_B^{*T} M_B + \delta F_B^T(\gamma - \gamma^*) \\ &+ \delta M_B^T(\kappa - \kappa^*) - \delta P_B^T(V_B - V_B^*) - \delta H_B^T(\Omega_B - \Omega_B^*)] dx_1 dt \\ &+\int_{t_1}^{t_2}\int_0^l \overline{\delta W} dx_1 dt = \overline{\delta A} \end{aligned} \tag{6}$$

To apply finite element discretization, the governing equation can be expressed in a simple form by using the simplest shape functions.

$$\begin{aligned} \delta\Pi_i = \int_0^l \Big\{ &\delta u_a'^T C^T C^{ab} F_B + \delta u_a^T \left[\left(C^T C^{ab} P_B\right)^\bullet + \tilde{\omega}_a C^T C^{ab} P_B\right] \\ &+ \overline{\delta\psi_a}'^T C^T C^{ab} M_B - \overline{\delta\psi_a}^T C^T C^{ab}\left(\tilde{e}_1 + \tilde{\gamma}\right) F_B \\ &+ \overline{\delta\psi_a}^T \left[\left(C^T C^{ab} H_B\right)^\bullet + \tilde{\omega}_a C^T C^{ab} H_B + C^T C^{ab}\tilde{V}_B P_B\right] \\ &- \overline{\delta F_a}^T \left[C^T C^{ab}\left(e_1 + \gamma\right) - C^{ab} e_1\right] - \overline{\delta F_a}'^T u_a \\ &- \overline{\delta M_a}^T \left[\left(\Delta + \frac{\tilde{\theta}}{2} + \frac{\theta\theta^T}{4}\right)\right] C^{ab}\kappa - \overline{\delta M_a}'^T \theta \\ &+ \overline{\delta P_a}^T \left[C^T C^{ab} V_B - v_a - \tilde{\omega}_a u_a\right] - \overline{\delta P_a}^T \dot{u}_a \\ &+ \overline{\delta H_a}^T \left(\Delta + \frac{\tilde{\theta}}{2} + \frac{\theta\theta^T}{4}\right) C\left(C^T C^{ab}\Omega_B - \omega_a\right) - \overline{\delta H_a}^T \dot{\theta} \\ &- \delta u_a^T f_a - \overline{\delta\psi_a}^T m_a \Big\} dx_1 \\ &- \left(\delta u_a^T \hat{F}_a + \overline{\delta\psi_a}^T \hat{M}_a - \overline{\delta F_a}^T \hat{u}_a - \overline{\delta M_a}^T \hat{\theta}\right)\Big|_0^l \end{aligned} \tag{7}$$

Where shape function is as follows:

(8) $$x = x_i + \xi \Delta l_i \quad dx = \Delta l_i d\xi \quad (\,)' = \frac{1}{\Delta l_i}\frac{d}{d\xi}(\,)$$

Through the mixed variational formulation, the resultant equations are expressed in a simple form as follows:

(9) $$F_S\left(X, \dot{X}\right) - F_L = 0$$

Where, F_S is the structural operator, F_L is the external force operator, and X is the unknown structural variables. For hingeless rotor blades, X is defined as follows:

(10) $$X = \left[\hat{F}_1^T, \hat{M}_1^T, u_1^T, \theta_1^T, F_1^T, M_1^T, P_1^T, H_1^T, ..., u_N^T, \theta_N^T, F_N^T, M_N^T, P_N^T, H_N^T, \hat{u}_{N+1}^T, \hat{\theta}_{N+1}^T\right]^T$$

For the time integration, a 2nd-order Euler backward method was adopted. To solve nonlinear equations simultaneously, a Newton-Raphson method was used. The present structural formulation is expressed in terms of the displacements, internal forces, and linear/angular momenta. Thus, the internal forces can be extracted directly from the beam solution.

2.2 CFD analysis

The equations governing three-dimensional, inviscid, unsteady, compressible flows are the Euler equations, which can be recast in an integral form for arbitrary computational domain V with boundary δV as

(11) $$\frac{\partial}{\partial t}\iiint_V \vec{Q} dV + \iint_{\partial V} \vec{F}(\vec{Q}) \cdot \vec{n} dS = 0$$

where $\vec{Q}$ is the vector of the conservative variables, and $\vec{F}(\vec{Q})$ represents the inviscid flux of these variables. The governing equations were discretized using a node-based finite-volume method. The inviscid flux was calculated based on Roe's flux-difference splitting scheme in a second-order accurate manner by applying a least-square reconstruction technique. A dual-time implicit time integration algorithm based on a linearized second-order Euler backward differencing was used to advance the solution in time. An unstructured overset mesh method [17] was utilized to treat the relative motion between the rotor blades and the fuselage. The mesh deformation due to blade deflection was taken care of by using a ball-vertex spring analogy method [18]. The flow solver was parallelized using MeTis and MPI libraries.

In Fig. 1, the computational mesh used for the HART II rotor CFD calculations is presented. The unstructured overset mesh is composed of a stationary background mesh block containing the fuselage, and four moving sub-blocks surrounding each individual blade. On the solid surfaces of the rotor blades and fuselage, triangular meshes were used. To better resolve the rotor wake, fine hexahedral cells were used around the rotor disk plane. The remaining region was mostly filled with tetrahedral cells that are connected to the hexahedrons with the pyramidal elements. The typical cell size in the wake region corresponds to 0.2 chord length at 75% blade span. The total number of cells used is 5,659,834, while the number of nodes is 1,369,025.

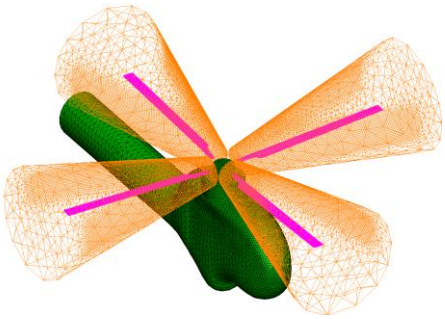

(a) Unstructured overset mesh

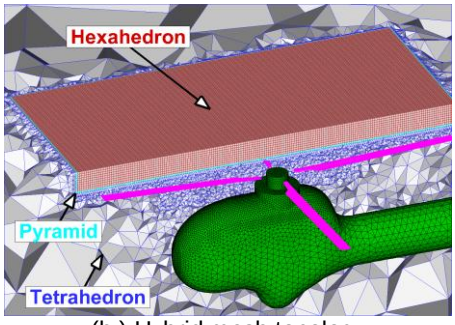

(b) Hybrid mesh topology

Figure 1. Unstructured overset computational mesh used for CFD calculations.

3. Numerical Results

The information of the HART II in wind tunnel trim condition is presented in Table 1. CSD analyses using the finite-state dynamic inflow model were first performed for the baseline case (BL), minimum noise case (MN), and minimum vibration case (MV) for validation. Then, the full CSD/CFD coupled analyses were to be executed.

However, the present CSD/CFD results for the BL case were obtained at the second coupled iteration step because the present coupled analyses are still ongoing. The final results will be given in the future.

Table 1. Information of HART II for wind tunnel test

Description	Symbol	Value
1) Rotor geometry :		
Rotor type		Hingeless
No. of blade	N_b	4
Radius	R	2m
Mean chord	c	0.121m
Solidity	σ	0.077
Airfoil		NACA23012mod
2) Operation condition:		
Rotational speed	Ω	109.12rad/s
Tip Mach	M	0.6387
Advanced ratio	μ	0.151
Thrust	T	3300N
Precone angle	β_p	2.5°
Shaft tilted angle	α_s	4.5° (aft)
3/rev pitch control	θ_{3p}	$\theta_{3p}= \theta_3 cos(3\psi+\varphi_3)$ θ_3=0.8°
For MN case		φ_3=300°
For MV case		φ_3=180°

3.1 Validation of CSD model

3.1.1 Rotor rotating frequencies

To validate the rotor blade modeling, fan plot was predicted and compared with the existing results. The rotating frequencies were extracted using transient time response by imposing sinusoidal waves up to 500Hz at the blade tip. Then, frequency domain results were obtained by using fast Fourier transform (FFT). The rotating speed was increased up to 1.2 times the nominal rotor speed. The rotating frequencies for the lowest six modes of the HART II rotor blade were presented in Fig. 2. The results of the rotating frequencies show good agreements with those in Ref. [2].

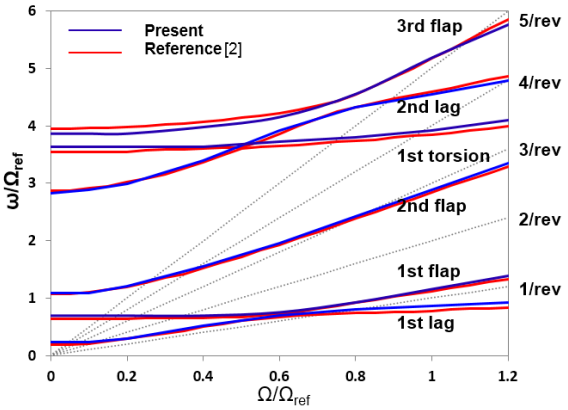

Figure 2. Fan plot results for HART II rotor blade

3.1.2 Trim results

Trim analyses were performed for the BL, MN, and MV cases, and the trim control angles were shown in Table 2. The predicted collective pitch angles for all cases are over-predicted compared to those of the measurement. But, the difference is less than 0.7˚. And the cyclic pitch angles are close to the measurement. Although the finite-state dynamic inflow model, which cannot capture the BVI phenomena, the present trim analyses are believed to be conducted successfully for the HART II wind tunnel test condition.

Table 2. The trimmed control angles

(a) BL case

	θ_0	θ_{1c}	θ_{1s}
Measurement	3.80	1.92	-1.34
Present	4.49	2.07	-1.74
Diff.(˚)	0.69	0.15	0.40

(b) MN case

	θ_0	θ_{1c}	θ_{1s}
Measurement	3.91	2.00	-1.35
Present	4.52	2.04	-1.32
Diff.(˚)	0.61	0.04	0.03

(c) MV case

	θ_0	θ_{1c}	θ_{1s}
Measurement	3.80	2.00	-1.51
Present	4.33	2.18	-1.76
Diff.(˚)	0.53	0.18	0.25

3.1.3 Blade deflection/ internal loads results

The elastic blade deflections at the tip were compared with those of measurement in the BL, MV, and MN cases. First, azimuthal variations of blade tip deflections for the BL case are shown in Figs. 3-4.

The present predicted flap deflection result shows an acceptable correlation with the measurement. But, the elastic twist is under-predicted than that of the measurement. However, the elastic twist was also under-predicted by the other CSD/CFD coupled analyses [4, 8]. And a phase lead was observed. This is because of the phase shift of the section normal force, which will be shown in the later section. For the MN and MV cases, in Figs. 5-8 the flap deflection results due to the 3/rev HHC input show good correlations with those of the measurement. But, the elastic twist results were also under-predicted, and a phase lead was observed, similar to the BL case. The mean values of the elastic twist are 1.0˚ lower than those of the measurement. But the fluctuating behavior shows a reasonable correlation with that of measurement.

The structural loads for both the present prediction and the measurement with flap bending moment and torsion moment measured at 0.17R and 0.33R are shown in Figs. 9-14. The mean value of each bending and torsion moments was subtracted in both the present results and the measurement. For the flap bending moments of BL, MN, and MV cases, the present results show a certain discrepancy with the measurement. This tendency was also shown in Ref. [3]. Thus, the present flap bending moment results show a reasonable correlation with those of the measurement. And the present torsion moments in the BL case shows a certain discrepancy with the measurement. But in the MN and MV cases, the difference of peak-to-peak value is less than 20% with that of the measurement. And a phase shift was observed with the difference of less than 15˚ with the measurement. But, the present results in the MN and MV cases show good correlations with the measurements.

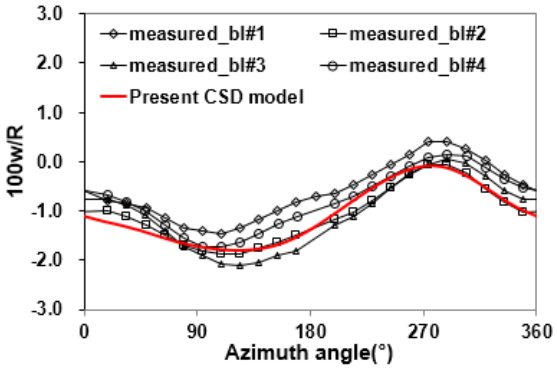

Figure 3. Flap deflection in BL case

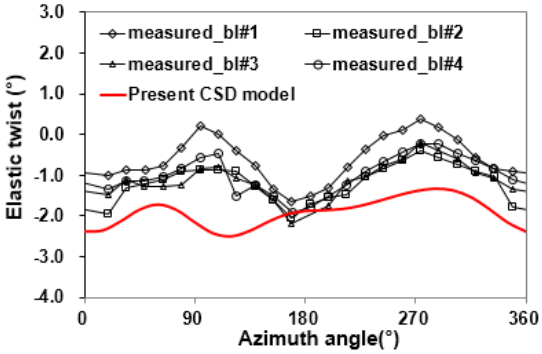

Figure 4. Elastic twist in BL case

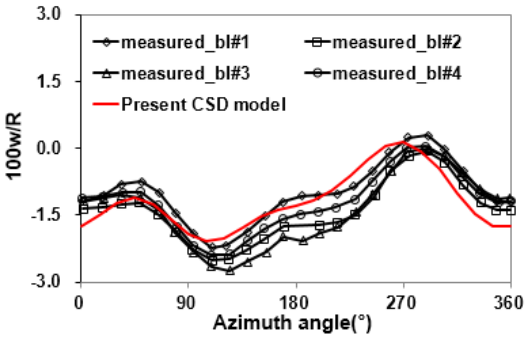

Figure 5. Flap deflection in MN case

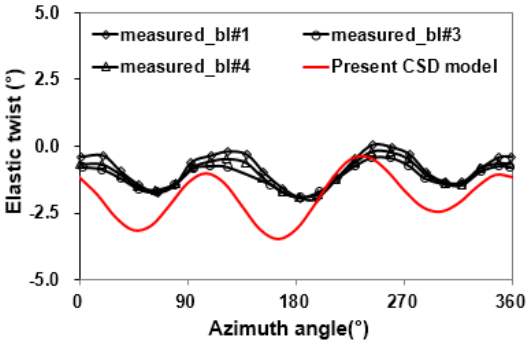

Figure 6. Elastic twist in MN case

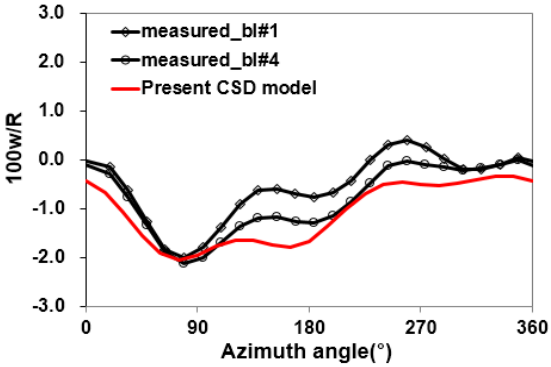

Figure 7. Flap deflection in MV case

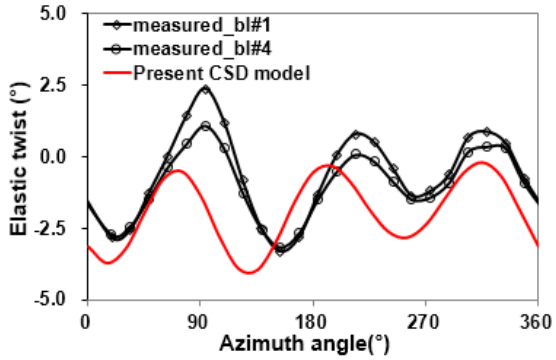

Figure 8. Elastic twist in MV case

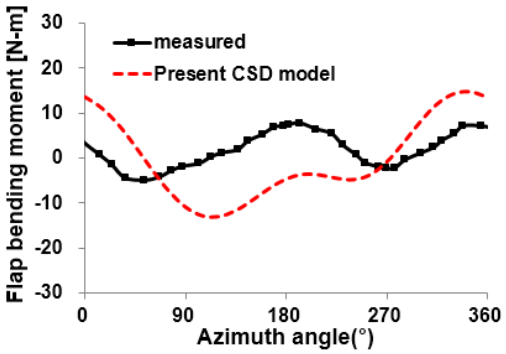

Figure 9. Flap bending moment in BL case

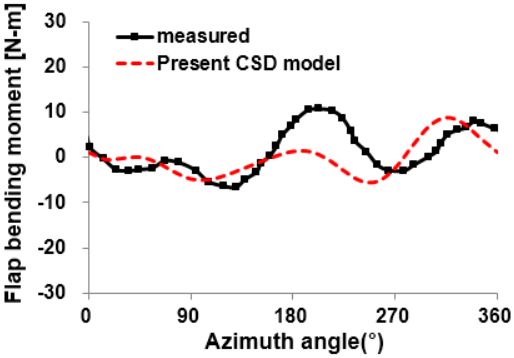

Figure 10. Flap bending moment in MN case

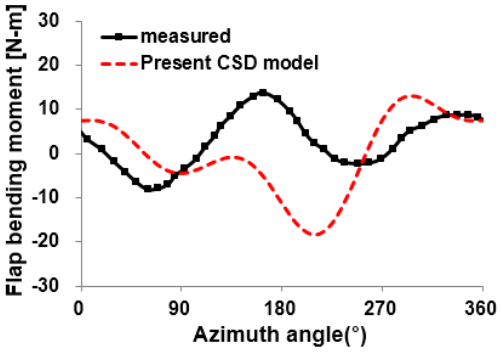

Figure 11. Flap bending moment in MV case

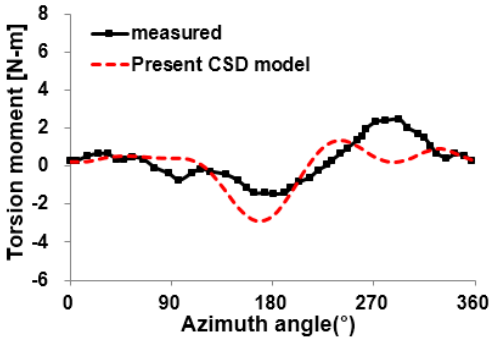

Figure 12. Torsion moment in BL case

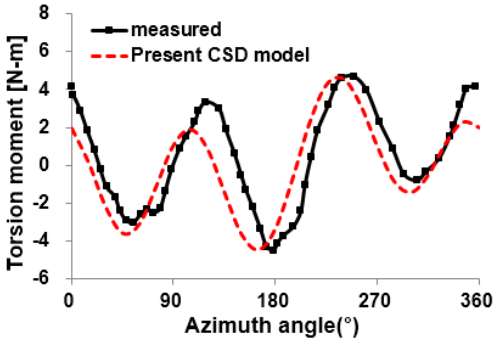

Figure 13. Torsion moment in MN case

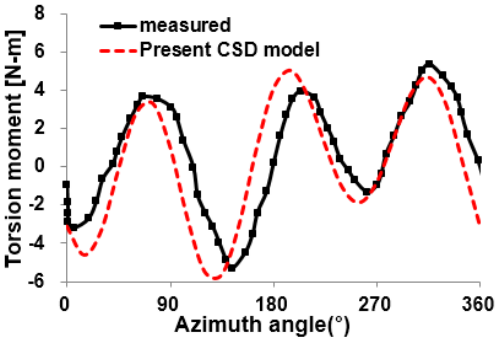

Figure 14. Torsion moment in MV case

3.1.4 Airloads results

The section normal force coefficient, C_nM^2 results obtained at 87% radial location for both present results and measurements are shown in Figs. 15-17. In the BL case, strong BVI events in the measurement at 0˚~90˚ in the advancing side and at 270˚ ~360˚ in the retreating side, as shown in Fig. 15. However, the present result using the finite-state dynamic inflow aerodynamics did not capture the BVI event since the induced inflow was calculated as simple harmonic functions. And a slight phase lead was observed as shown in the elastic twist results. Although the BVI phenomena was not captured and the phase lead was observed by the present results, general tendency in the section normal force

coefficient, C_nM^2 shows a reasonable correlation with that of measurement.

In the MN and MV cases, C_nM^2 fluctuation becomes significant than in the BL case since 3/rev HHC input. And a slight phase lead was observed, but the present result shows a similar tendency with that of measurement. The comparison of the airloads results for both the present CSD model using the finite-state dynamic inflow model and CSD/CFD coupled analysis will be discussed in next section.

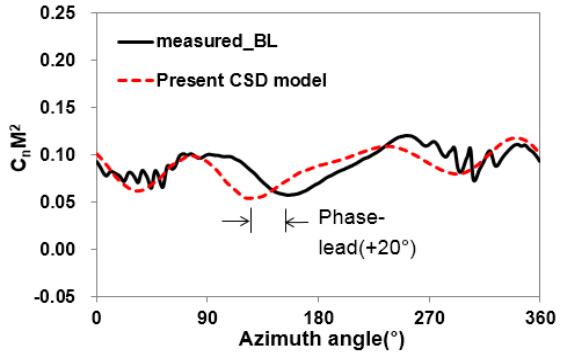

Figure 15. Section normal force, C_nM^2 in BL case

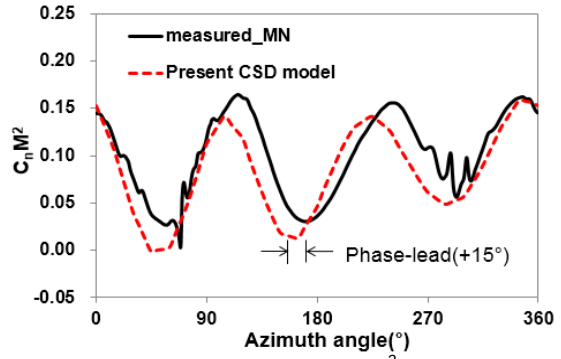

Figure 16. Section normal force, C_nM^2 in MN case

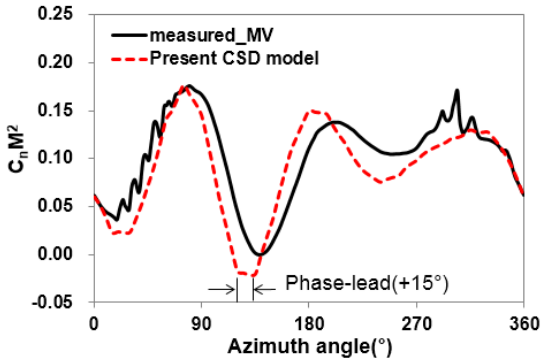

Figure 17. Section normal force, C_nM^2 in MV case

3.3 CSD/CFD coupled analysis

In the present CSD/CFD coupled analysis, structural deflection and blade airload results are examined and discussed in Figs. 18-20. For the flap deflection, the CSD/CFD coupled analysis predicts well the behavior in the first quadrant as compared to the CSD prediction using the finite state dynamic inflow model. However, in the elastic twist results, CSD/CFD coupled result was under-predicted compared to the present CSD model. But, the tendency of the elastic twist behavior shows a good agreement with the measurement. And the elastic twist results in both the present CSD and CSD/CFD analysis were observed obviously in Ref. [3-4].

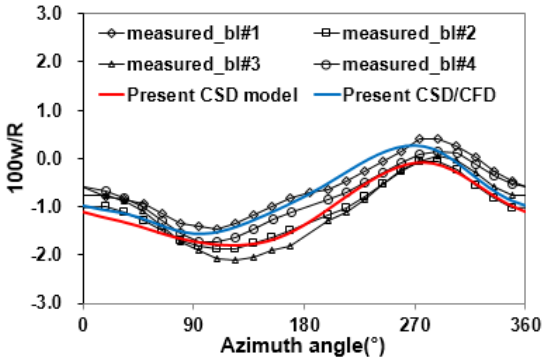

Figure 18. The comparison of flap deflection in BL case

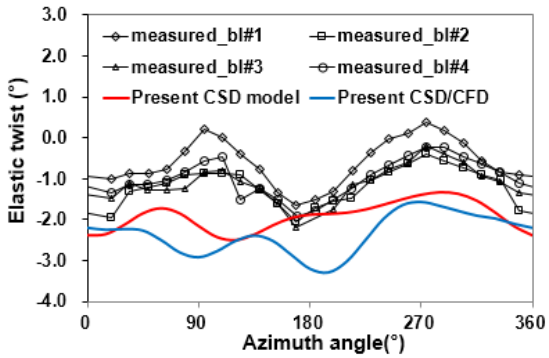

Figure 19. The comparison of the elastic twist in BL case

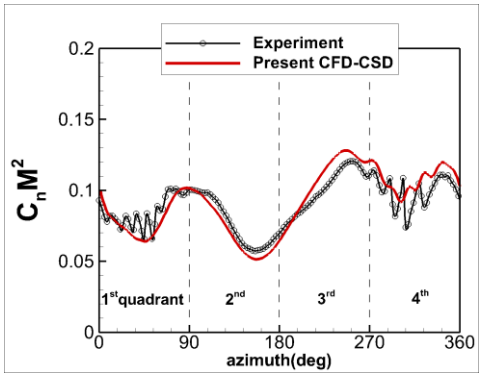

(a) Normal force coefficient

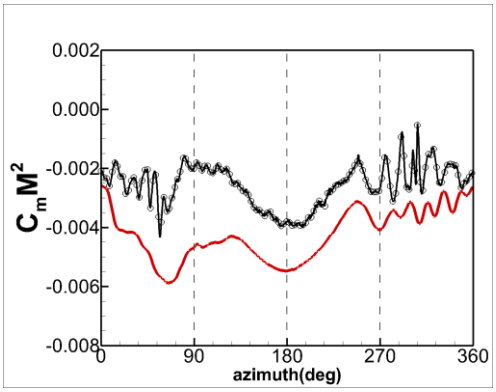

(b) 1/4-chord pitching moment coefficient

Figure 20. Azimuthal variations of normal force and 1/4-chord pitching moment coefficients at 87% blade span.

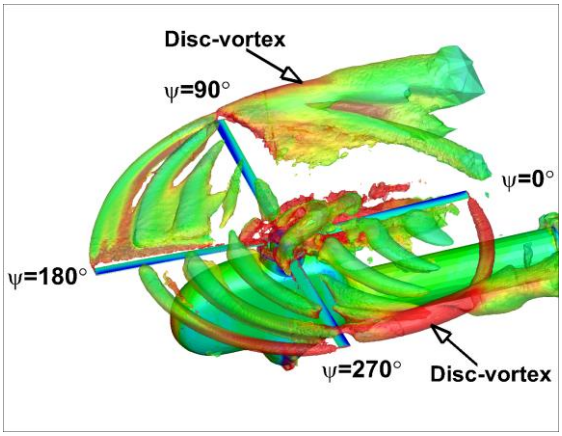

Figure 21. Rotor wake structure represented by iso-λ_2 surface colored with vorticity magnitude when the reference blade is located at zero azimuth angle.

In Fig. 20, the azimuthal variations of normal force and 1/4-chord pitching moment coefficients at 87% radial location were presented, along with the experimental measurement. Overall, the unsteady behaviors of the blade airloads were in a good agreement with the measurement, even though the high-frequency BVI loadings at the rear portion of the rotor disk were not well captured, particularly at the 1st quadrant. This is mainly because the computational meshes were not dense enough for resolving the rotor wake without excessive numerical dissipation. Also, the under-predicted mean value for the pitching moment is believed to be due to the assumption of inviscid flows.

In Fig. 21, the rotor wake structure represented by iso-λ_2 surface was presented when the reference blade is located at zero azimuth angle. It is shown that the tip vortices remain very close to the rotor disk plane, and a pair of disc-vortices is formed at the lateral edges of the rotor disk. Because the blades strongly interact with those vortices, particularly at the 1st and 4th quadrants, the BVI loadings were created as indicated in Fig. 20. Also, the tip vortices in the advancing side was less well-defined than those in the retreating side, causing poor prediction of the BVI loadings at the 1st quadrant.

Conclusions

This paper presents the aeromechanical analysis for the HART II rotor using both a CSD model and a CSD/CFD coupled analysis. The present CSD model adopted a mixed variational geometrically exact beam formulation. And the present CSD combined with the finite-state dynamic inflow aerodynamics were adopted to analyze rotor aeroelasticity. In the present CSD model using only the finite-state dynamic inflow, the BVI phenomena in the section normal force, C_nM^2 , cannot be captured. But the general tendency for the BL, MN, and MV cases showed an acceptable correlation with those in the measurement. And the trimmed control angles show difference of less than 0.7˚ with the measurement. In the structural results, the flap deflections in all three cases show acceptable correlations with the measurement. But, the elastic twist results were under-predicted and a phase lead that was closely related to the phase of the section normal force was observed. Tendencies showed a reasonable correlation with the measurement. In structural loads results, flap bending moments of all the cases show a certain discrepancies with the measurement. However, torsion moments show similar tendency with the measurement.

In the numerical results by the full CSD/CFD coupled analysis, more accurate results were obtained compared to the CSD model using the finite -state dynamic inflow. Although the BVI events were still not well captured due to the numerical dissipation of the rotor wake, the blade airloads are in a better agreement with the measurement. Also, the flap deflection and the elastic twist were predicted more precisely. In this paper, the CSD/CFD coupled analysis results were presented at the second coupled iteration step since the coupled analysis is still ongoing. In the future, the finally converged results will be presented. Also, instead of the inviscid Euler calculations, Navier-Stokes CFD calculations will be performed for more precise prediction.

Acknowledgements

This work was supported by the National Research Foundation (NRF) grant funded by the Korean government (2011-0029094). Also, this work was supported by Advanced Research Center Program (No. 2013073861) through the National Research

Foundation of Korea (NRF) grant funded by the Korea government (MSIP) contracted through Advanced Space Propulsion Research Center at Seoul National University. And the authors thank the HART II team for the test results.

References

[1] B. G. van der Wall, 2nd HHC Aeroacoustic Rotor Test (HART II) - Part I: Test Documentation -, Institute Report IB 111-2003/31, German Aerospace Center (DLR), Braunschweig, Germany, 2003.

[2] B. G., Van der Wall, 2nd HHC Aeroacoustic Rotor Test (HART II) - Part II: Representative Results -, Institute Report IB 111-2005/03, German Aerospace Center (DLR), Braunschweig, Germany, 2005.

[3] B. G. van der Wall, J. W. Lim, et al., An Assessment of Comprehensive Code Prediction State-of-Art Using the HART II International Workshop Data, *American Helicopter Society International 68th Annual Forum*, TX, May, 2012.

[4] M. J. Smith, et al., An Assessment of CFD/CSD Prediction State-of-Art Using the HART II International Workshop Data, *American Helicopter Society International 68th Annual Forum*, Texas, May, 2012.

[5] R. T. Biedron, and E. M. Lee-Rausch, Rotor airloads Predictions Using Unstructured Meshes and Loose CFD/CSD coupling, 26th AIAA Applied Aerodynamics Conference, August, 2008.

[6] T. Simth, and C. E. S. Cesnik, Numerical Investigation of Integral Twist Actuation for BVI Noise Reduction, *American Helicopter Society International 62nd Annual Forum*, Phoenix, Arizona, May, 2006.

[7] J.-S. Park, and S. N. Jung, Comprehensive Multibody Dynamics Analysis for Rotor Aeromechanics Predictions in Descending Flight, *The Aeronautical Journal*, 116 (1177) (2012) 229-249

[8] J. W. Lim, and A. C. B. Dimanlig, An Investigation of the Fuselage Effect for HART II Using a CFD/CSD Coupled Analysis, *Proc. of the American Helicopter Society Specialist's Meeting, 2nd International Forum on Rotorcraft Multidisciplinary Technology*, Seoul, Korea, October, 2009.

[9] M. Amiraux, J. D. Baeder, and S. N. Koushik, Improved Correlation with the HART-II Rotor Test Data using Coupled CSD/CFD and Three Levels of Numerical Modelization, *Proc. of the 38th European Rotorcraft Forum, Amsterdam, Netherlands*, September, 2012.

[10] J.-S. Park, Multibody Analyses for Performance and Aeromechanics of a Rotor in Low-speed Flight, *Aircraft Engineering and Aerospace Technology*, 86 (2) (2014) 33-42.

[11] M. Potsdam, H. S. Yeo, and W. Johnson, Rotor Airloads Prediction using Loose Aerodynamic/Structural Coupling, *American Helicopter Society International 60th Annual Forum*, Baltimore, MD, June, 2004.

[12] W. Johnson, CAMRAD II, Comprehensive Analytical Model of Rotorcraft Aerodynamics and Dynamics, Johnson Aeronautics, Palo Alto, California, 1992-2005.

[13] G. Bir, et al., University of Maryland Advanced Rotor Code (UMARC): Theory Manual, Technical Report UM-AERO94-18, Center for Rotorcraft Education and Research, University of Maryland, College Park, July, 1994.

[14] O. A. Bauchau, DYMORE Users' Manual, School of Aerospace Engineering, Georgia Institute of Technology, Atlanta, GA, May 2006.

[15] D. H. Hodges, A Mixed Variational Formulation based on Exact Intrinsic Equations for Dynamics of Moving Beams, *International Journal of Solids and Structures*, 26 (11) (1990) 1253-1273.

[16] D. A. Peters, and C. J. He, Finite State Induced Flow Models Part II: Three-Dimensional Rotor Disk, *Journal of Aircraft*, 32 (2) (1995) 1493-1511.

[17] Jung, M. S., Kwon, O. J., "A Parallel Unstructured Hybrid Overset Mesh Technology for Unsteady Viscous Flow Simulations," International Conference of Computational Fluid Dynamics, Antalya, Turkey, 2007.

[18] Bottasso, C. K., Detomi, D., Serra, R., "The Ball-Vertex Method: A New Simple Spring Analogy Method for Unstructured Dynamic Meshes," Computer Methods in Applied Mechanics and Engineering, vol. 197, pp. 4244-4264, 2005.